J Appl Physiol
89: 323–337, 2000.

Detailed flow patterns in the nasal cavity

J. T. KELLY, A. K. PRASAD, AND A. S. WEXLER
Department of Mechanical Engineering, University of Delaware, Newark, Delaware 19716-3140

Received 27 May 1999; accepted in final form 24 January 2000

Kelly, J. T., A. K. Prasad, and A. S. Wexler. Detailed flow patterns in the nasal cavity. *J Appl Physiol* 89: 323–337, 2000.—The human nasal cavity filters and conditions inspired air while providing olfactory function. Detailed experimental study of nasal airflow patterns has been limited because of the complex geometry of the nasal cavity. In this work, particle image velocimetry was used to determine two-dimensional instantaneous velocity vector fields in parallel planes throughout a model of the nasal cavity that was subjected to a nonoscillatory flow rate of 125 ml/s. The model, which was fabricated from 26 computed tomography scans by using rapid prototyping techniques, is a scaled replica of a human right nasal cavity. The resulting vector plots show that the flow is laminar and regions of highest velocity are in the nasal valve and in the inferior airway. The relatively low flow in the olfactory region appears to protect the olfactory bulb from particulate pollutants. Low flows were also observed in the nasal meatuses, whose primary function has been the subject of debate. Comparison of sequentially recorded data suggests a steady flow.

particle image velocimetry; nasal airflow; human; replica model

THE HUMAN NASAL CAVITY filters, warms, and humidifies inspired air. It also houses the sensitive nerve fibers that are responsible for olfaction (3). By acting as a filter, the nasal cavity protects the lungs from the deleterious effects of inspired particulate and vapor pollutants. In the process, however, the nasal cavity places itself at risk from these insults. A detailed characterization of nasal airflow patterns, which largely influence inspired particle trajectories, and, therefore, deposition patterns, is required to understand local transport and deposition in the nasal cavity and to determine the pollutant concentration introduced to the lungs.

The compact size and complex geometry of the nasal cavity has made the detailed experimental study of nasal airflow challenging. Early attempts at in vivo observations of airflow were unsatisfactory and provided conflicting results. Swift and Proctor (22) made the first quantitative in vitro velocity measurements by inserting a miniature Pitot device into the flow passage of a model that was made from the nasal cast of a cadaver. To aid visualization, the model approximated the nasal septum with a transparent, flat, plastic plate. Flow visualization of a dye, which was injected outside the nostril into a steady flow of water, indicated that the major proportion of flow passed through the middle airway. A small fraction of the flow separated upward, forming a standing eddy in the olfactory area. The flow was found to be laminar at a flow rate of 125 ml/s. Turbulent flow was detected downstream of the nasal valve at a flow rate of 208 ml/s. These experiments were limited by *1*) the approximate geometry due to both the flat septum and variations between cadavers and live subjects, which result from postmortem shrinkage of tissue, *2*) the use of a Pitot device, which is an invasive technique that yields pointwise velocity measurements, and *3*) the small size of the cast model.

Girardin et al. (4) used laser Doppler velocimetry, a noninvasive technique, to determine the velocity of water droplets suspended in air flowing through a nasal model made from a nasal cast of a cadaver. Measurements were made at five coronal cross sections for a flow rate of 166 ml/s. Large velocities were found near the septum in the lower portion of the model. Although an improvement over previous work, it was limited to pointwise velocity measurements. Again, the geometry was approximated with a flat plate for a nasal septum and limited by the use of a cadaver.

Hornung et al. (7) studied the flow of ^{133}Xe through a life-size model of a nasal cavity generated from a nasal cast of a cadaver. This study confirmed the results of earlier visualization experiments (10, 20) by finding the majority of flow to be in the lower nasal airways and an increasing proportion of flow in the olfactory region at elevated flow rates. However, because of the small size of the model, detailed flow patterns were not determined. The model was also limited by the tissue variations between cadavers and live subjects.

Schreck et al. (18) studied the flow in a ×3 enlarged plastic model generated from magnetic resonance images (MRI), spaced in 4-mm increments, of a decongested subject. Templates were formed from scaled MRI data and were cut into Plexiglas plates, which were assembled to form the nasal model. Flow visualizations indicated that two vortexes form just posterior to the nasal valve during inspiration. A relatively large vortex formed in the upper part of the model, and smaller one formed along the nasal floor. Pointwise

Address for reprint requests and other correspondence: A. S. Wexler, Mechanical Engineering, Univ. of Delaware, Newark, DE 19716-3140 (E-mail: wexler@me.udel.edu).

The costs of publication of this article were defrayed in part by the payment of page charges. The article must therefore be hereby marked "*advertisement*" in accordance with 18 U.S.C. Section 1734 solely to indicate this fact.

velocity measurements, made with a hot-wire anemometer, indicated that the majority of the flow passed through the central part of the passages, while smaller fractions passed through the meatuses and the olfactory slit. Detailed flow patterns, however, were not determined.

Hahn et al. (5) constructed a ×20 scaled replica of a nasal cavity from computerized axial tomography (CAT) scans recorded in 2-mm increments from the tip of the naris to the beginning of the nasopharynx. The outlines of scaled CAT scan data were cut out of Styrofoam slabs, which were then glued together to form the nasal model. Pointwise velocity measurements made in five planes throughout the model with a hot-film anemometer indicated that the flow was laminar at flow rates up to around 200 ml/s. It was found that ~50% of inspired air flows through the combined middle and inferior airways and ~14% through the olfactory region at all flow rates studied.

Park et al. (14) were the first to use a two-dimensional measurement technique, digital particle image velocimetry (PIV), to study nasal airflow patterns. A ×3 scaled nasal replica was generated from approximately nine coronal slices of anatomic data (from nostril to nasopharynx) taken from Ref. 10. The resulting vector plots show a significant portion of high-velocity flow in the olfactory region. The limitations of this work are the low-resolution anatomic data used for model generation and the merging of vector plots in five sublocations of each study plane to form the global velocity field. The Park and co-workers' results stand alone in their observation of high-velocity flow in the olfactory region.

In this work, PIV is used to determine two-dimensional velocity fields in a ×2 scaled replica of a human right nasal cavity that was created by using rapid prototyping techniques. Twenty-six coronal slices of anatomic data from the external naris to the nasopharynx were used for model creation, and the merging of vector plots in two sublocations per study plane was performed.

MODEL CREATION

The major challenge in the experimental study of nasal airflow is the accurate reproduction of the complex anatomy of the nasal passages in a model conducive to noninvasive fluid mechanical experiments (i.e., creation of an anatomically accurate model in an optically transparent material). The complex nasal anatomy determines the flow patterns in the airway; therefore, an accurate replication of the anatomy is imperative.

Figure 1 illustrates the nasal anatomy and the commonly used nomenclature, proposed by Proctor (16). Inspired air enters the nasal cavity through the nasal valve, a slitlike opening of small cross-sectional area, after passing through the external naris, or nostril. At the posterior end of the nasal valve, there is an abrupt increase in cross-sectional area marking the beginning of the region referred to as the main nasal passages. The main nasal passages are largely formed by projections of cartilage and bone referred to as conchas, or turbinates, and extend to the posterior end of the cavity. A novel model creation technique, described in detail in Ref. 6, was employed to create the scaled replica and is briefly described here.

Given the roughly symmetric anatomy of the nasal cavities and the cyclic pattern of nasal breathing, only one of the two nasal cavities was studied. Twenty-six computed tomography scans of the right nasal cavity, from the posterior end of the external naris to the nasopharnyx, of a normal 25-yr-old man were recorded and digitized for further processing (Fig. 2). Digitized cross-sectional data were scaled and lofted together in the IDEAS Master Series solid modeling package to form a ×2 scaled solid model (Fig. 3). A low-resolution three-dimensional version

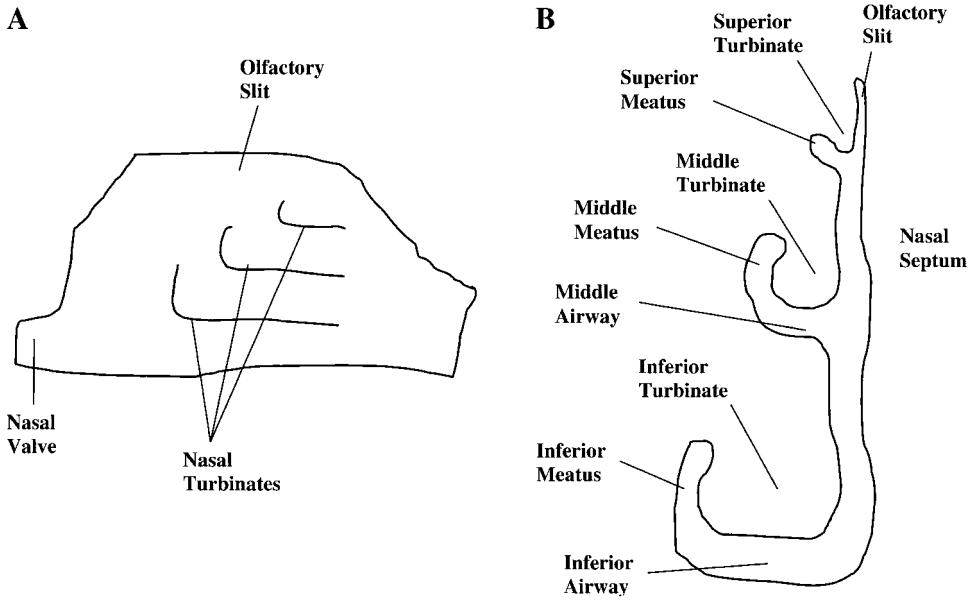

Fig. 1. Anatomy of the sagittal (*A*) and coronal (*B*) planes of the nasal cavity.

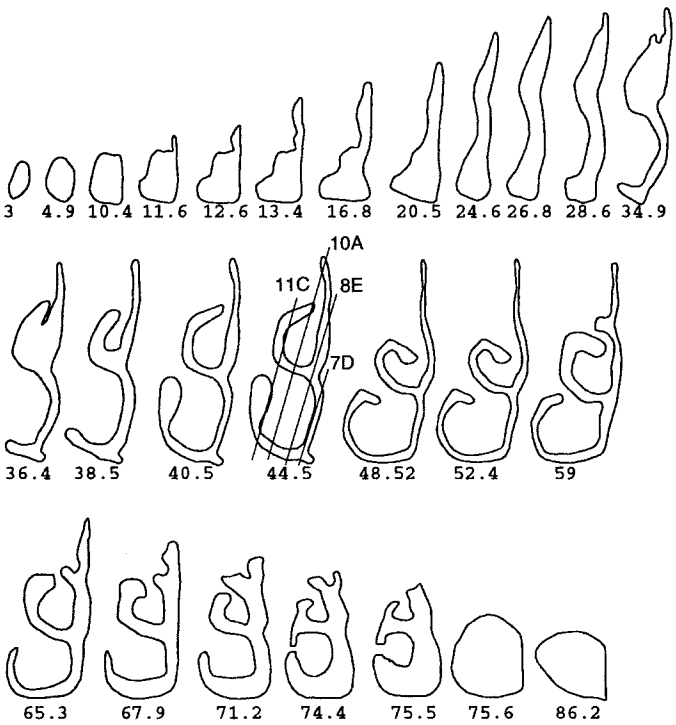

Fig. 2. Coronal computed tomography scan data of a 25-yr-old male right nasal passage. Numbers indicate distance (in mm) from the posterior end of the naris (0 mm) to the termination of the passage (86.2 mm). Locations of Figs. 7*D*, 8*E*, 10*A*, and 11*C* are indicated on the coronal plane 44.5 mm from the naris.

of this model is available on-line in VRML 2.0 at http://www.me.udel.edu/wexler/asw.be.html. The model, which describes the "negative" of the nasal geometry, was rapidly prototyped in a water-soluble cornstarch material by using a three-dimensional printer (http://www.Zcorp.com). The corresponding "positive" was obtained by embedding the prototype in clear plastic and subsequently dissolving it in water. The resulting model (see Fig. 6) is an anatomically correct representation of a $\times 2$ scale right nasal cavity embedded in clear silicone (Sylgard 184, Dow Corning).

Some possible shortcomings of the model are *1*) the inlet to the nasal cavity is an approximately horizontal tube that does not accurately model the curved shape of a nostril, *2*) nostril hairs are not included in the replica, and *3*) the silicone model does not have the warm, moist, and compliant properties of nasal tissue.

The vestibule of the nose is at a slight angle differing from the horizontal when the head is positioned in the erect posture. This angle is variable, and in some persons it offers a nearly horizontal opening (16). The quasi-funnel shape of the vestibule is believed to homogenize the flow distribution at the nasal valve, thereby eliminating the influence of the nostril shape on downstream flow patterns. Considering this, the inlet tube of the model may not significantly compromise the accuracy of flow data. However, this remains to be determined.

Concerning the absence of nasal hairs in the model, Hahn et al. (5) determined that velocity profiles in selectively studied locations of a $\times 20$ scaled nasal replica were little affected by the inclusion of nasal hairs. Through examination of the Grashof and Prandtl numbers and use of a heat and mass transport analogy, Hahn et al. also showed that the thermal/water properties of the nasal tissue do not significantly alter the flow during typical breathing conditions.

EXPERIMENTAL METHOD

PIV, a technique for measuring fluid velocities over global domains, was used to obtain two-dimensional instantaneous velocity vector fields in parallel planes throughout the nasal model. In brief, a fluid seeded with tracer particles is pumped through the optically transparent material model. The tracer particles are illuminated twice in rapid succession by a pulsed sheet of laser light and are recorded photographically. Hence, two subsequent positions of each particle with a known time separation are obtained. Postprocessing yields two- or three-dimensional instantaneous velocity vectors within the illuminated plane (1, 15).

Figure 4 is a schematic diagram of the PIV apparatus. In our application, the working fluid was a mixture of glycerol and water. The index of refraction of the mixture was matched to that of the silicone model to avoid refraction of the laser sheet while it passed through the convoluted surfaces of the flow passage and to eliminate the resulting distortion of the image field. This matching resulted in an optimal mixture of 59% glycerol-41% water by volume.

A rotating mirror (General Scanning) was used for image shifting to resolve the directional ambiguity problem that arises from reverse flows in some portions of the model. Velocity vectors were obtained from particle displacements determined by a cross-correlation operation. A resolution of 2.8 mm in the model, or 1.4 mm in the human counterpart, was provided by overlapping adjacent interrogation spots by 50%. Given the resolution of the charge-coupled device camera (Kodak ES 1.0, 1,000 $\times$ 1,000 pixels) in relation to the size of the flow passage, images were recorded from two locations in each plane, and vector maps were joined after interrogation. The model was positioned on an *XY*-translation stage that allowed the images to be recorded in parallel planes spaced 1 mm apart.

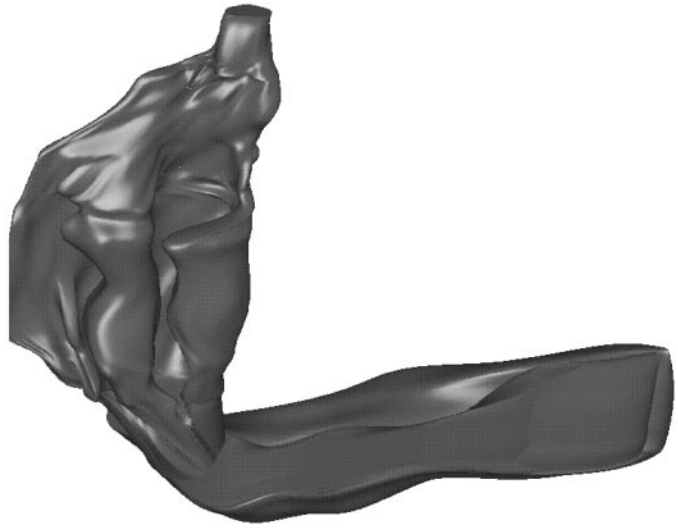

Fig. 3. Solid computer model of the nasal passage and its relation to the pharynx.

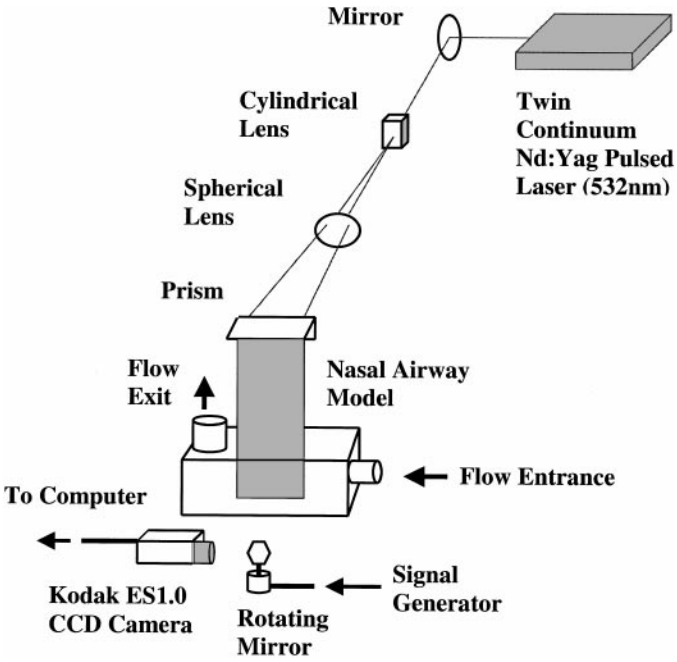

Fig. 4. Schematic diagram of the particle image velocimetry apparatus. CCD, charge-coupled device.

As a result of the choice of working fluid and the scale of the airway, the Reynolds number was matched to that of a human breathing air to ensure kinematic similarity. This matching amounts to

$$\dot{Q}_{\text{Mixture}} = 2\,\frac{\nu_{\text{Mixture}}}{\nu_{\text{Air}}}\,\dot{Q}_{\text{Air}} \qquad (1)$$

where $\mathring{V}\dot{Q}$ is the volume flow rate and ν is the kinematic viscosity.

At 27.5° C, the kinematic viscosity of the glycerol-water mixture is 6.55×10^{-6} m^2/s (10). When a kinematic viscosity of 16×10^{-6} m^2/s is used for air, and a flow rate of 125 ml/s, which is a typical resting breathing rate, the necessary glycerol-water volume flow rate is 103 ml/s. This flow rate was maintained by using a Vanton Flex-I-Liner pump, which produces a pulseless flow, and was measured with a Kings Instrument 7511 flowmeter as shown in Fig. 5.

RESULTS

Figures 7–11 are vector plots of the flow in sagittal planes throughout the model. The flow was pumped in the right-to-left direction at a steady flow rate equivalent to that of air flowing through a life-size model at 125 ml/s. At this flow rate, the flow in the model is laminar. Figure 7*A* is a plane slightly offset from the nasal septum, and subsequent planes are spaced in 1-mm increments. The approximate position of the flow passage in the model is shown in Fig. 6, which is in the coronal plane of the airway. The model is at a slight angle to the sagittal plane; this fact should be kept in mind when viewing the vector plots. The locations of several sagittal planes are indicated in Fig. 2.

Figure 7 details the flow in the lower part of the nasal cavity in planes close to the nasal septum. As a result of the nonplanar shape of the nasal septum, Fig. 7, *A* and *B*, depict regions of the flow that are adjacent

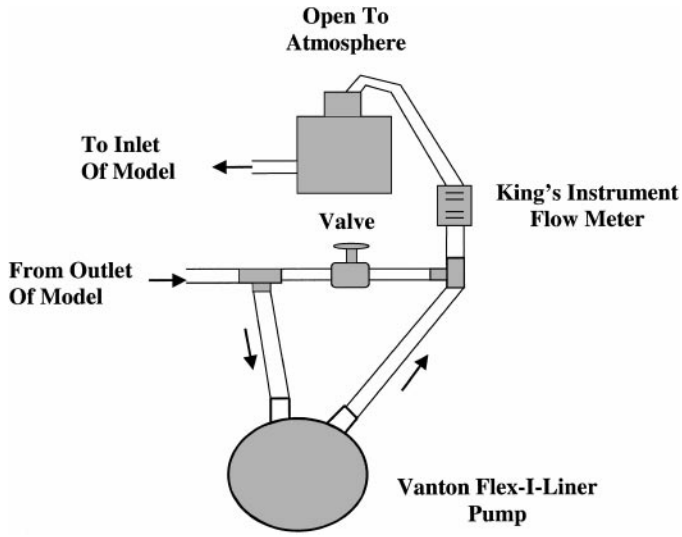

Fig. 5. Schematic diagram of the flow control apparatus.

to, slightly offset, and still in contact with the septal wall. The left side of these plots shows an area of negligible velocity adjacent to the septum. Despite the pumping of fluid in the right-to-left direction, the low-velocity flow on the right side is primarily directed toward the upper part of the plot, and there is also a reversed flow in this region. This deviation in direction from the main flow is a result of the fluid in this region being proximate to the septal wall. Figure 8*E*, for example, which depicts a plane further offset from the wall, shows a flow in a parallel region that is predom-

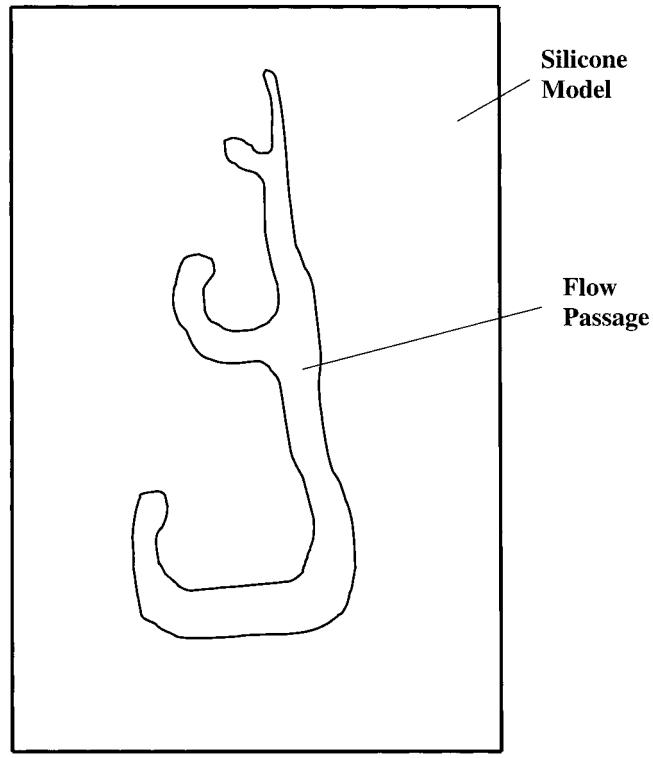

Fig. 6. Schematic diagram of the nasal model.

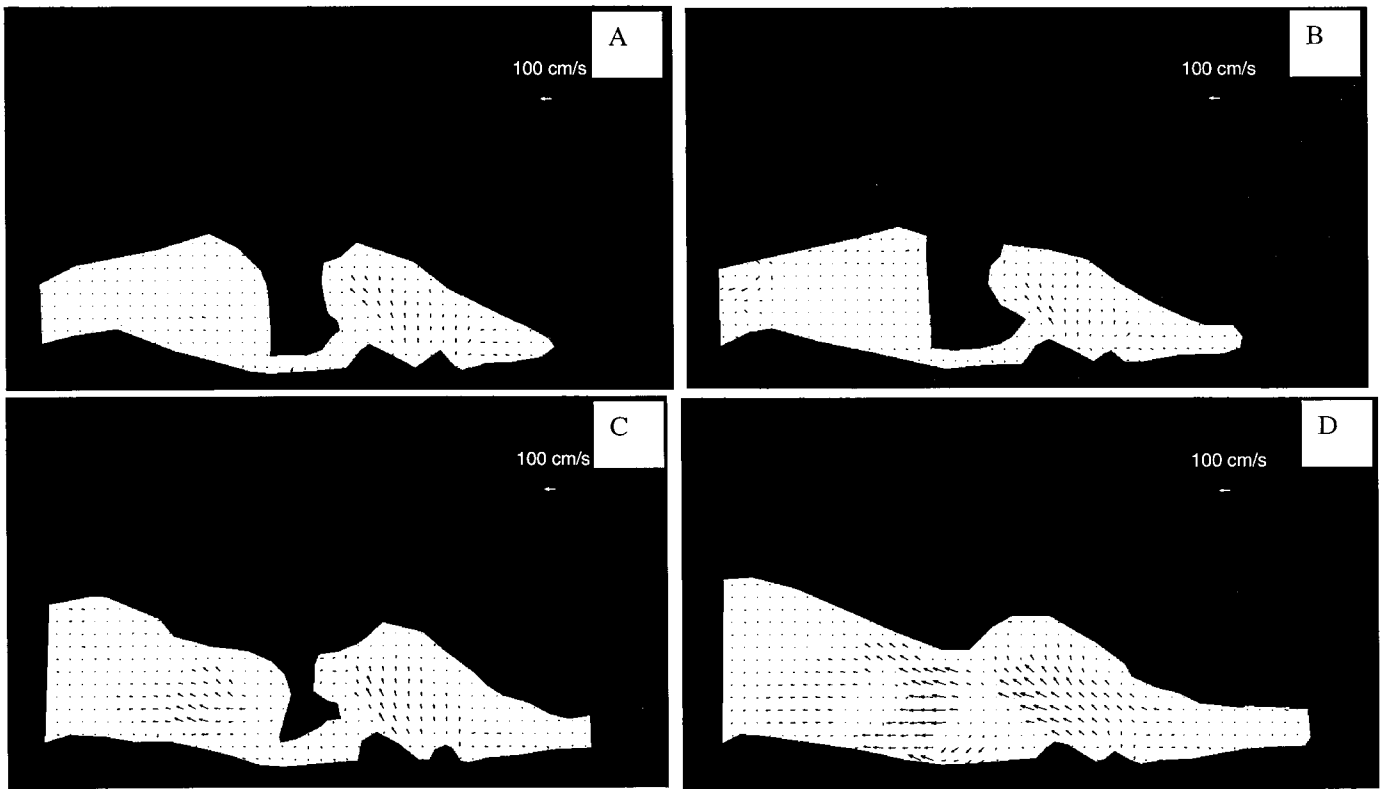

Fig. 7. Plots of two-dimensional instantaneous velocity vectors, in air, in planes parallel to the nasal septum and spaced in 1-mm increments, corresponding to an air flow rate of 125 ml/s. Figure 7*A* is in the plane closest to the septum, and Fig. 11*J* is the farthest.

inantly in the right-to-left direction. Figure 7*C* depicts a region of flow along the septal wall at a depth of about two-thirds of the nasal cavity. The reverse flow seen in Fig. 7, *A* and *B*, is also visible in Fig. 7*C* but is less pronounced in Fig. 7*D*, in which region the flow has a more uniform direction. The flow along the septal wall that was noticed in Fig. 7*C* is also present in Fig. 7*D*; however, there is a region in its center where the velocity is very small. This is a result of the plane of study being adjacent to the inferior turbinate in this location.

The images in Fig. 8, which are further offset from the septum, show higher velocities than in Fig. 7, *A–D*. Figure 8, *A* and *B*, depicts the flow separating around a region of low velocity that is adjacent to the inferior turbinate. In Fig. 8, *C–E*, this separation is more pronounced, and the branch of the flow below the inferior turbinate (in the inferior airway) is moving at a higher velocity. Figure 8*E* is in the plane of the olfactory slit and shows very little flow in the olfactory region. Because of its small cross-sectional area, the nasal valve experiences a high-velocity flow in this plane.

Figure 9 depicts an eddy in the anterior part of the cavity. This is evident in Fig. 9*A* as a flow separation and reversed flow just posterior to the nasal valve. In Fig. 9, *B* and *C*, further from the septal wall, this reversed flow is clearly an eddy. This eddy is a result of the adverse pressure gradient caused by the abrupt increase in cross-sectional area from the nasal valve to the main nasal passage. Schreck et al. (18) observed two eddies in this expansion region; however, the size and location of those eddies were different than those of the one seen here. This discrepancy is probably due to anatomic differences between the models. In addition to the eddy, Fig. 9, *B–E*, shows the appearance of the middle turbinate, and Fig. 9*F* shows the superior turbinate. Notice in all of these panels that there is very little flow in the olfactory slit.

Figure 10 shows the region of the nasal valve and, just posterior, the "pinch off" from the rest of the flow passage. An eddy can be seen in this area in Fig. 10*D*. The geometry of this region is apparent in Fig. 3 as the small bulge near the floor of the cavity just posterior to the nasal valve.

Figure 11, *A–J*, shows the area of the pinched off region gradually diminishing and disappearing. These panels progress through the planes of the inferior, middle, and superior meatuses. Very little flow reaches these airways as is seen for example in Fig. 11, *F* and *G*.

ERROR ANALYSIS

Fluid tracking. The fluid velocity was obtained by determining the velocity of "tracer" particles (60-μm hollow glass spheres), which were assumed to track the flow. There are two forces relevant to this experiment

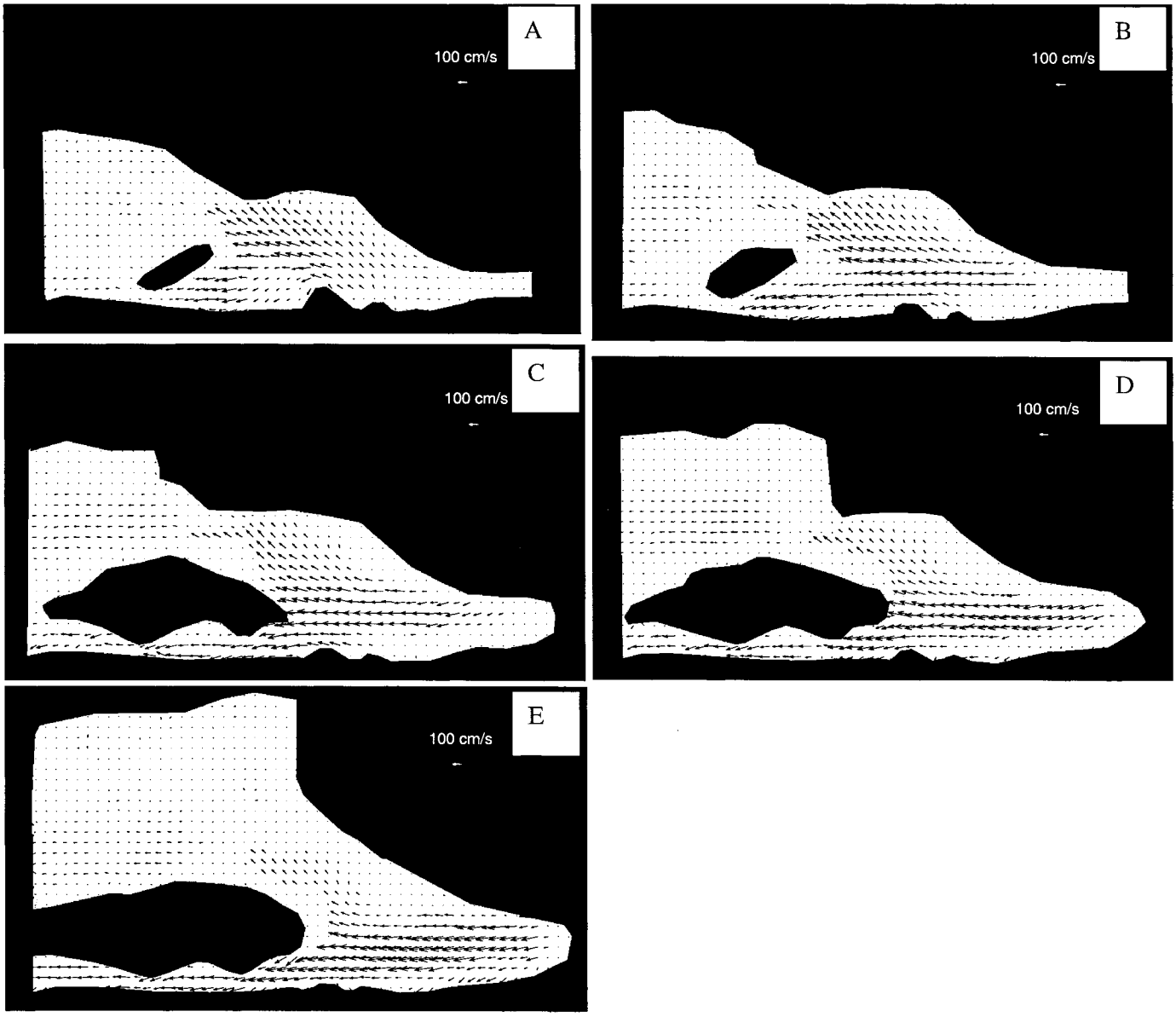

Fig. 8. See legend to Fig. 7.

that cause the particle motion to deviate from that of the fluid: gravitational forces and inertial forces. To investigate the ability of the particles to track the flow, we used the Stokes approximation to determine the velocity difference between the particles and the fluid, as follows

$$(u_p - u) = \frac{(\rho_p - \rho)\, D_p^2}{18\mu}\left(\frac{du_p}{dt} - g\hat{z}\right) \qquad (2)$$

where u_p is the particle velocity, u is the fluid velocity, ρ_p is the particle density, ρ is the fluid density, μ is the absolute viscosity, D_p is the particle diameter, g is the gravitational acceleration, and $\hat{z}$ is the unit vector in the vertical direction.

Comparing the gravitational acceleration, 9.8 m/s^2, with the largest particle acceleration observed, 3.8 m/s^2 (the acceleration of the particle in glycerol-water, not air), it is found that the gravitational term is more dominant. The particle acceleration, approximated as $u_p^2/\Delta x$, where Δx is the vertical or horizontal spacing between neighboring vectors, was determined in a region of high-velocity gradient (the region where the flow impinges on the inferior turbinate in Fig. 8*D*). Considering that the gradient in this region is significantly larger than the gradients in the majority of the flow domain, the tracking infidelity caused by particle inertia is probably negligible compared with that caused by gravitational forces in most regions.

Neglecting the particle acceleration and using ρ_p = 600 kg/m^3, ρ = 1,150 kg/m^3, $D_p = 60 \times 10^{-6}$ m, and $\mu = 7.55 \times 10^{-3}$ kg·m^{-1}·s^{-1}, the slip velocity is 0.14 mm/s. Considering that the velocities in the low-flow regions, such as the olfactory slit, are about 3–10 mm/s, the particles track the flow to within about 5% even in low-velocity regions.

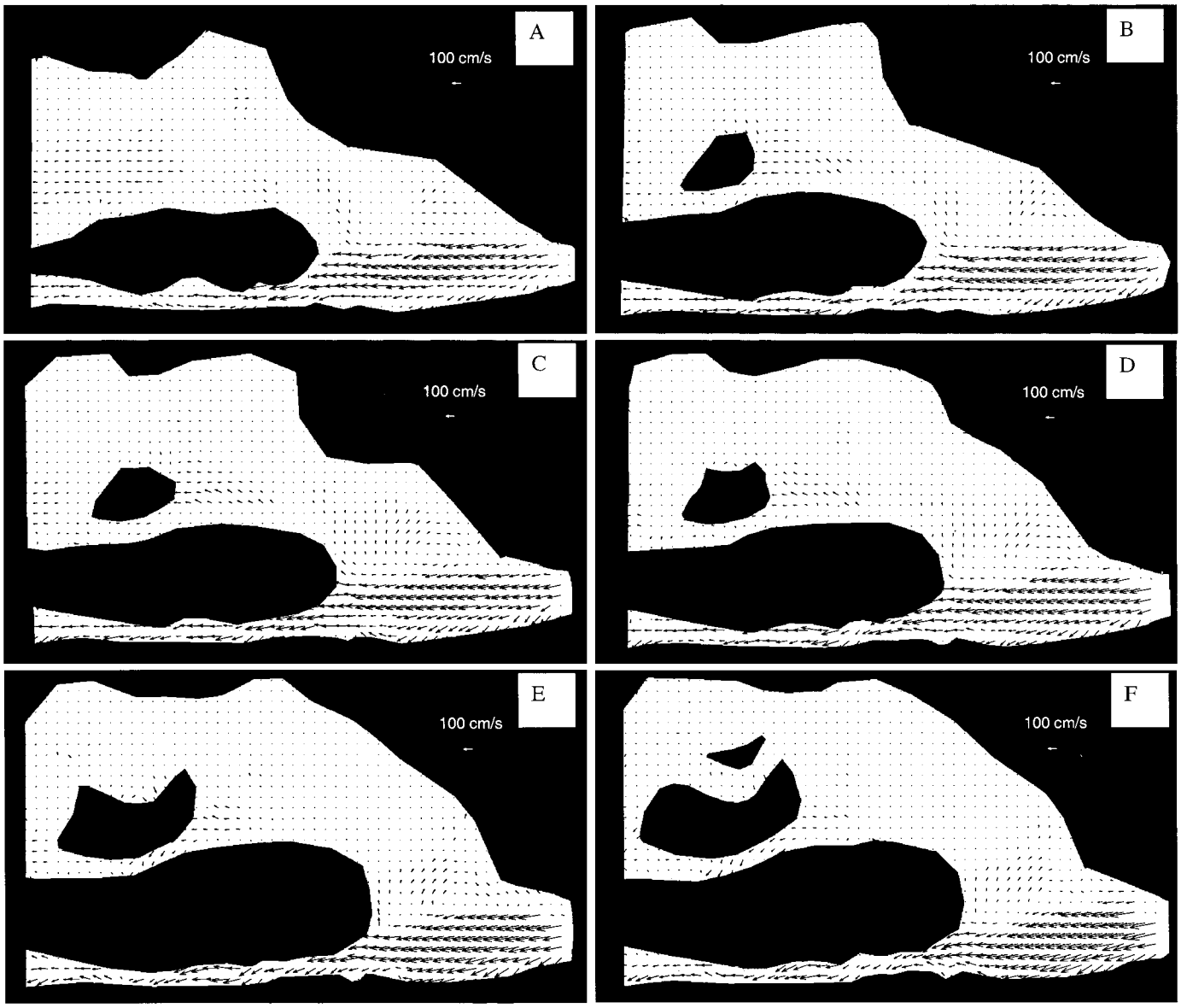

Fig. 9. See legend to Fig. 7.

Vector cleaning. Each interrogation spot yields a single vector located by the highest peak in the cross-correlation field (the domain containing signal peaks the intensities of which correspond to the degree of correlation). Occasionally, however, the highest peak might correspond to a noise spike, and, therefore, the locations of three additional peaks of decreasing height are stored during the interrogation process. During vector cleanup, it is sometimes necessary to replace the vector corresponding to the highest peak with one of the three alternate choices. Approximately 14% of the total number of vectors were replaced. Approximately 57% of these (8% of the total) were resolved by replacing the faulty vector with a vector corresponding to the second, third, or fourth strongest correlation signal peak. The remaining 43% (6% of the total) were interpolated from neighboring data.

The errors can be attributed to the following reasons. *1*) There are a few air bubbles trapped in the nasal model that preclude accurate data from being acquired in small regions of the affected planes. *2*) Despite the apparent transparent optical properties of silicone, the nasal model has a slight amber tinge and attenuates the scattered light from flow particles to a small degree. *3*) To capture the entire flow domain in two images, a lower magnification was used than is ideally desirable. This caused the image of some flow passages, such as the inferior and middle airways, to be a narrow slit. Because of a small amount of light scatter on interfacial surfaces, there is a larger error associated with flow near a wall. Hence, a narrow slit, in which the majority of the flow is near a wall, will have a greater percentage of error than a larger airway.

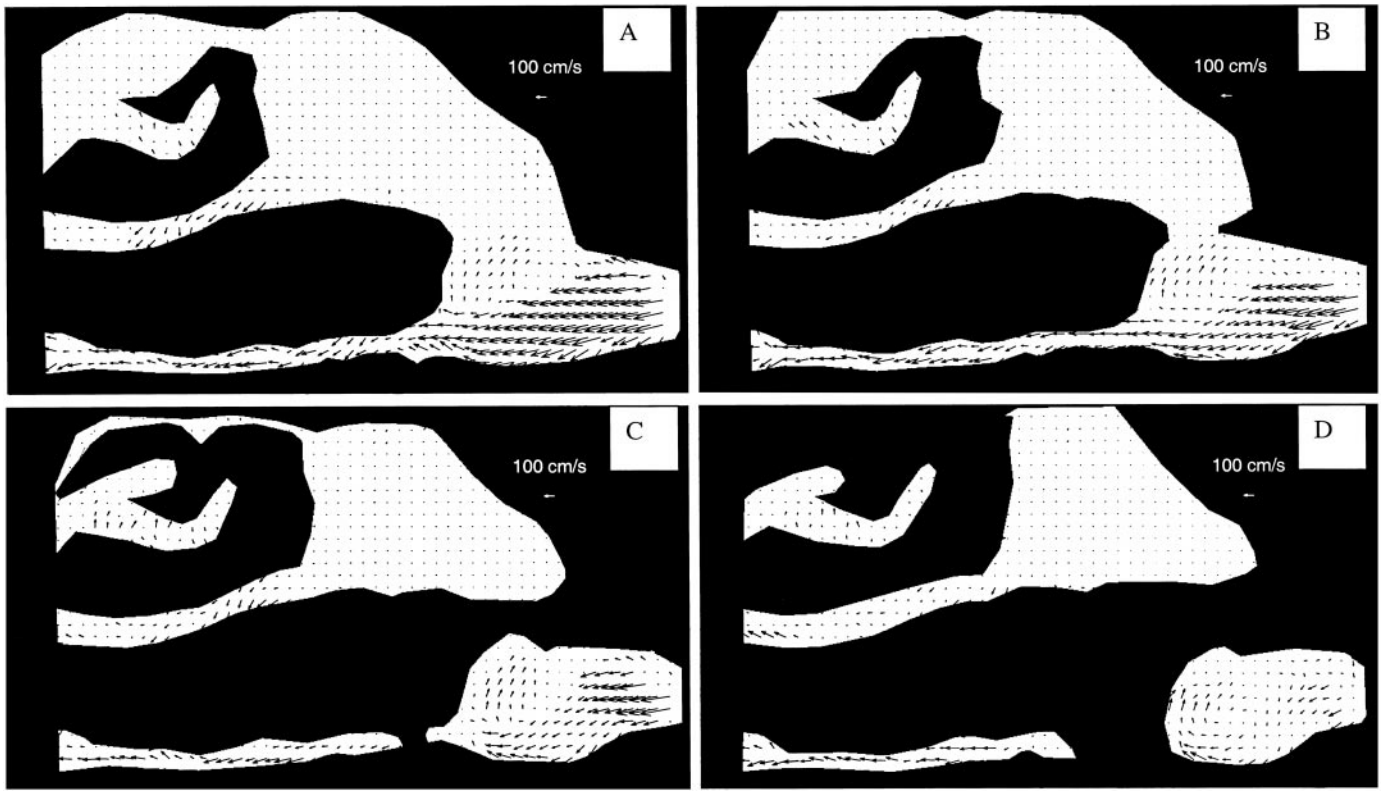

Fig. 10. See legend to Fig. 7.

To ensure judicious choices when cleaning the raw data, vectors were inspected manually. If a vector significantly deviated from the mean flow in the passage, its corresponding location in the photographic image was examined. The probable cause of the error in this location was then noted (i.e., bubble obstruction, wall region, or a random error). Next, vectors corresponding to the second, third, and fourth signal peak were substituted and compared with the mean flow. If none of these vectors was a suitable replacement, an interpolation was done. In areas in which a portion of the flow region was obstructed by an air bubble in the model, vector substitution was often futile, and an interpolation was performed. In narrow slitlike airways, vector substitution usually proved successful. In these areas, vectors were substituted on the basis of data that had been acquired previously at a higher magnification, in addition to considering the local mean flow. This method is believed to be prudent because of the steady nature of the flow, which is discussed below. The area of most uncertainty was the middle airway, and more study of this location may prove useful.

Image merging. Images were recorded from two sublocations per study plane. These images were interrogated separately, and resulting vector plots were merged to form the global velocity field. The recording of images from two locations in each plane requires the model to be translated parallel to the laser sheet. Deviation from this direction because of improper alignment of the translation stage or model would cause the two images to be recorded in slightly different planes and would result in associated error. To evaluate this error, the absolute difference of velocities between the two coplanar vector plots was calculated in regions in which they overlap. The resulting error vectors for a representative sample of data are plotted in Fig. 12. The error vectors in Fig. 12, *A*–*D*, describe the error induced by merging the vector plots that form Fig. 8, *B*–*E*, respectively. The error vectors resulting from merging vector plots to form Figs. 9*F* and 10, *A* and *B*, are plotted in Fig. 12, *E*–*G*, respectively.

The upper halves of the error vectors plotted in Fig. 12, *A* and *B*, show that the error is primarily random and small. However, there is a pattern to the error vectors in the lower part of the plot (i.e., there appears to be a small right-to-left velocity). This pattern can be understood by examining Fig. 8, *B* and *C*. There is a significant difference in velocity between the planes of Fig. 8, *B* and *C*, in the location at which the pattern of error was noticed in Fig. 12, *A* and *B*. Considering the 1-mm spacing between planes, this represents a large velocity gradient in the out-of-plane dimension. Consequently, even a small out-of-plane translation of the model would result in the observed error.

Similar logic explains the error vectors plotted in Fig. 12, *C* and *D*. There is a pattern of error vectors in the central region of the plot. These error vectors appear to be a flow separating around the inferior turbinate. Notice that there is a large velocity gradient between the planes of Figs. 8*D*, 8*E*, and 9*A* in this location resulting from the presence of the inferior turbinate. The consequence of this gradient is that a

small deviation of the model from the required translation direction would cause a large error.

Comparison of the error vectors in Fig. 12, *E–G*, with velocity data in Figs. 9*F* and 10, *A* and *B*, also shows the pattern of the error vectors to be correlated with the velocity gradient in the out-of-plane dimension. In Fig. 12, *E–G*, there is very little error in the region above the inferior turbinate. Examination of Figs. 9*F* and 10, *A* and *B*, in this region shows that the velocity difference is small between these planes. Larger gradients in the out-of-plane dimension do exist below the turbinate, however, and there is a larger associated error.

Steady state. The validity of merging vector plots corresponding to images acquired at different times depends on the temporal fluctuations of the flow, in addition to issues previously discussed. To investigate the error incurred from merging sequentially recorded data, velocity data from images recorded in the same location at different times were subtracted, and the resulting error vectors were plotted.

Figure 13 shows representative plots of the absolute difference in velocity between two images taken in the same region at different times. Figure 13, *A* and *B*, corresponds to the planes of the vector plots in Fig. 8, *D* and *E*, respectively, and Fig. 13, *C–E*, to those of Figs. 9, *E* and *F*, and 10*A*, respectively.

Examination of Fig. 13, *A* and *B*, shows the flow to be reasonably steady. The error vectors in most regions are small with the exception of those in the inferior airway and in the region just posterior to the nasal valve. Comparison of Fig. 13, *A* and *B*, with Fig. 8, *D* and *E*, respectively, reveals that the large errors occur in regions where the velocity gradient is large. For example, the errors in Fig. 13, *A* and *B*, just posterior to the nasal valve occur in locations where high-velocity flow in Fig. 8, *D* and *E*, abruptly transitions to a low-velocity flow along a wall. The errors in the inferior airway, which is relatively narrow, are near the walls where there is also a large velocity gradient. Notice the flow above the inferior turbinate on the left side of Fig. 8, *D* and *E*. There is a relatively small velocity gradient associated with this flow because of its gradual transition to low-velocity flow. Fig. 13, *A* and *B*, shows small error vectors in this region.

Comparison of Fig. 13, *C–E*, with Figs. 9, *E* and *F*, and 10*A*, respectively, further confirms that the large errors occur where the velocity gradients are high. In the central region of the nasal valve and just posterior, where there is a high velocity but low-velocity gradient in Figs. 9, *E* and *F*, and 10*A*, there is very little error in Fig. 13, *C–E*. In the location where this high velocity abruptly transitions to negligible velocity, however, there is a larger error. Narrow flow passages, such as the middle and inferior airway, by nature have high-velocity gradients, and there is greater error in those locations in Fig. 13, *C–E*.

These disagreements can be explained by considering the velocity gradients in an interrogation spot (the finite region in which flow particle data are averaged to obtain a local particle displacement), in an area of large error, and a characteristic length scale of an interrogation spot. An estimate of the local error due to velocity gradients can be obtained by multiplying the velocity gradient in an interrogation spot by the spot's characteristic length scale. With the use of one of the interrogation spot's dimensions for a characteristic length, the error estimate reduces to Δv, the difference between velocities in the region of interest.

Comparison of the difference in velocity across large velocity gradients in Figs. 8, *D* and *E*, 9, *E* and *F*, and 10*A* with the errors in Fig. 13, *A–E*, respectively, shows that Δv is of the same order of magnitude as the errors. This result, along with the observation that the disagreements occur only in regions of high-velocity gradients, suggests that the disagreements are an artifact of the finite discretization and are not actual flow phenomena.

This analysis has shown the flow to be predominantly steady in nature. Disagreements between the sequential flow measurements coincide only with large velocity gradients. This indicates that the flow is steady.

Errors relative to local velocity magnitude. Considering that the flow is steady, sequentially recorded data may be used to determine the location of errors with magnitudes that are large relative to the magnitudes of their respective velocity vectors. To this end, the squared differences of the components of velocity vectors, obtained from data acquired in the same plane at two different times, were added, and the result was divided by the average of the squares of the two corresponding vector lengths, in the following way

$$\text{Error} = \left\{ \frac{(u_{t1} - u_{t2})^2 + (v_{t1} - v_{t2})^2}{\tfrac{1}{2}[(u_{t1}^2 + v_{t1}^2) + (u_{t2}^2 + v_{t2}^2)]} \right\}^{1/2} \qquad (3)$$

where u_{t1} and u_{t2} represent the components of velocity in the pumping direction (right to left in Figs. 7–14) at two different times, $t1$ and $t2$, respectively, and v_{t1} and v_{t2} represent the components of velocity, normal to the pumping direction, at times $t1$ and $t2$, respectively.

Errors calculated in this way are plotted in Fig. 14 for a representative sample of data. The reference vector illustrates the length of an error vector that represents a velocity difference equal to the average local vector length (i.e., a value of 1.0 in *Eq. 3*). Note that the error "vectors" represent magnitudes only, and their directions have been arbitrarily chosen to be from right to left.

Comparison of Fig. 14, *A* and *B*, with Fig. 8, *D* and *E*, respectively, and Fig. 14, *C–E* with Figs. 9, *E* and *F*, and 10*A*, respectively, reveals that the large errors correspond to regions of low-velocity flow. Notice the major regions of flow in Fig. 8, *D* and *E*. There is high-velocity flow in the region posterior to the nasal valve and in the inferior airway, and a moderate velocity flow in a region along the septal wall above the inferior turbinate. Examination of these regions in Fig. 14, *A* and *B*, shows that there is a very small error associated with them. Now, compare the regions of low-velocity flow in Fig. 8, *D* and *E* (the uppermost part of the plot, regions proximate to the inferior turbinate,

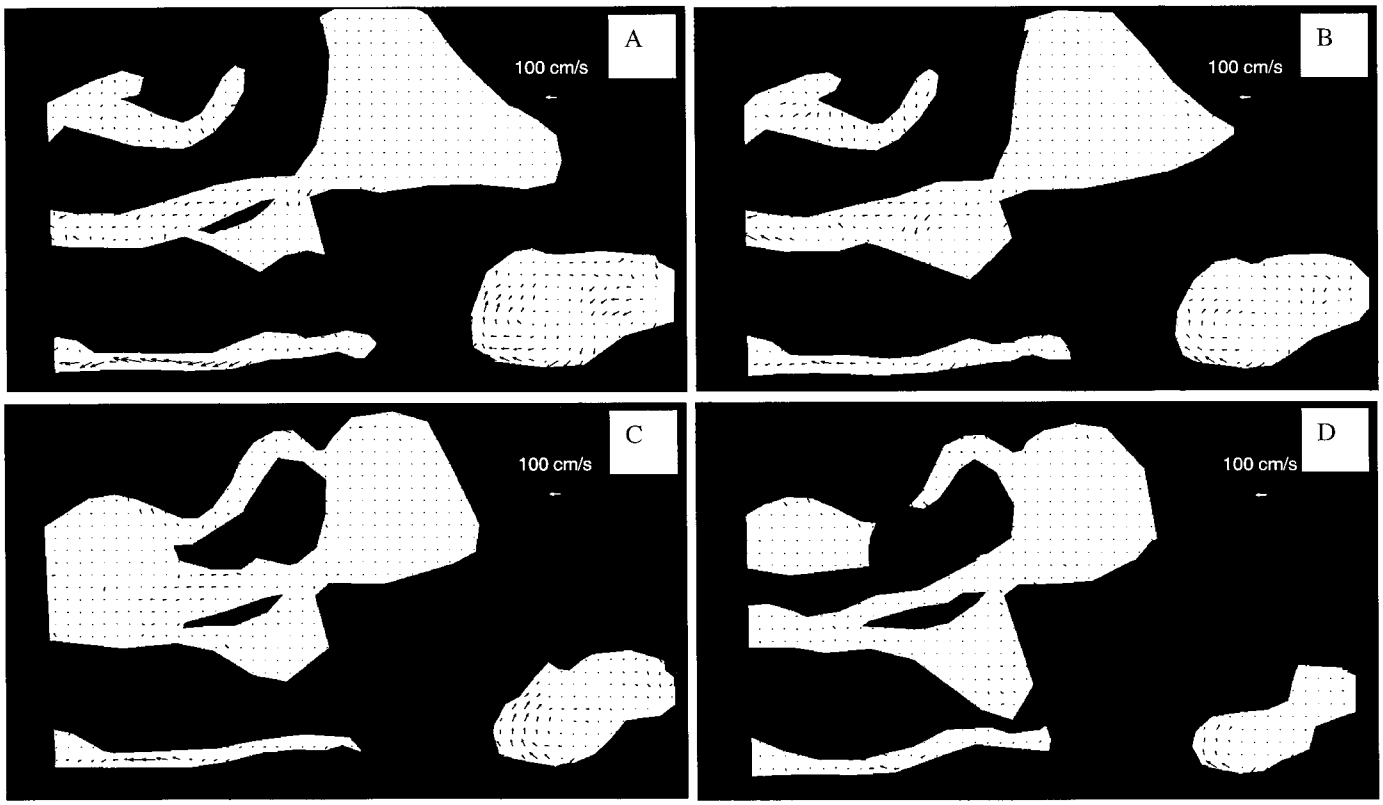

Fig. 11. See legend to Fig. 7.

and wall regions in the upper right half of the plot), with the corresponding regions in Fig. 14, *A* and *B*, respectively, and notice that regions of low velocity have a larger error associated with them.

Comparison of Fig. 14, *C–E*, with Figs. 9, *E* and *F*, and 10*A*, respectively, yields the same conclusion. The regions of high velocity in Figs. 9, *E* and *F*, and 10*A* (the nasal valve and just posterior, and the inferior airway) correspond to regions of small error in Fig. 14, *C–E*. The regions of low velocity in Figs. 9, *E* and *F*, and 10*A* (large portions of the upper half of the plots) are plagued with larger errors in Fig. 14, *C–E*.

The explanation for this phenomenon is that the small velocity vectors corresponding to regions of high error represent velocities that are approaching the level of experimental detection. This is supported by the result that the errors associated with larger velocities, which were in the range of detection, were found to be insignificant compared with their respective vector length.

The primary importance of studying flow patterns in the nasal cavity is to determine their physiological implication. In very-low-velocity regions, where the large errors were found, the transport and deposition mechanisms do not significantly depend on the flow patterns. Particles entering the low-flow regions will generally be ultrafine particles, or particles of an aerodynamic diameter <100 nm, whose transport is dominated by Brownian diffusion. Hence, a detailed characterization of flow in these stagnant regions may not be necessary to understand the region's function.

DISCUSSION

There are several prominent flow features in Figs. 7–11 that are worth special attention: *1*) there is very little flow in the olfactory slit; *2*) there is very little flow in the meatuses; and *3*) the highest velocities are at the nasal valve and in the inferior airway.

The relatively small flow in the olfactory slit has been observed to varying degrees in other experimental studies (4, 5, 7, 18, 20, 22). This phenomenon is a logical consequence of the small cross-sectional area of the olfactory slit relative to that of the lower nasal airways. The low-flow characteristic seems to be a defense mechanism that prevents particles whose trajectories are heavily dependent on flow patterns from being convected to and deposited on the sensitive olfactory nerve fibers, while allowing vapors to diffuse to that region for olfaction. Because of the narrow shape of the airway, the ultrafine particles, whose transport is dominated by diffusion, will generally deposit in a lower part of the airway.

Stuiver (20) reported in his visualization experiments that 5–10% of the inspired air passed through the olfactory slit for normal inspiration rates. Hornung et al. (7) generally confirmed these results. Hahn et al. (5) found that ~14% of the flow passed through the olfactory slit independent of flow rate. The results presented here are for a single flow rate, 125 ml/s, which is on the low side of a typical resting breathing rate (125–200 ml/s). The plots show a smaller fraction

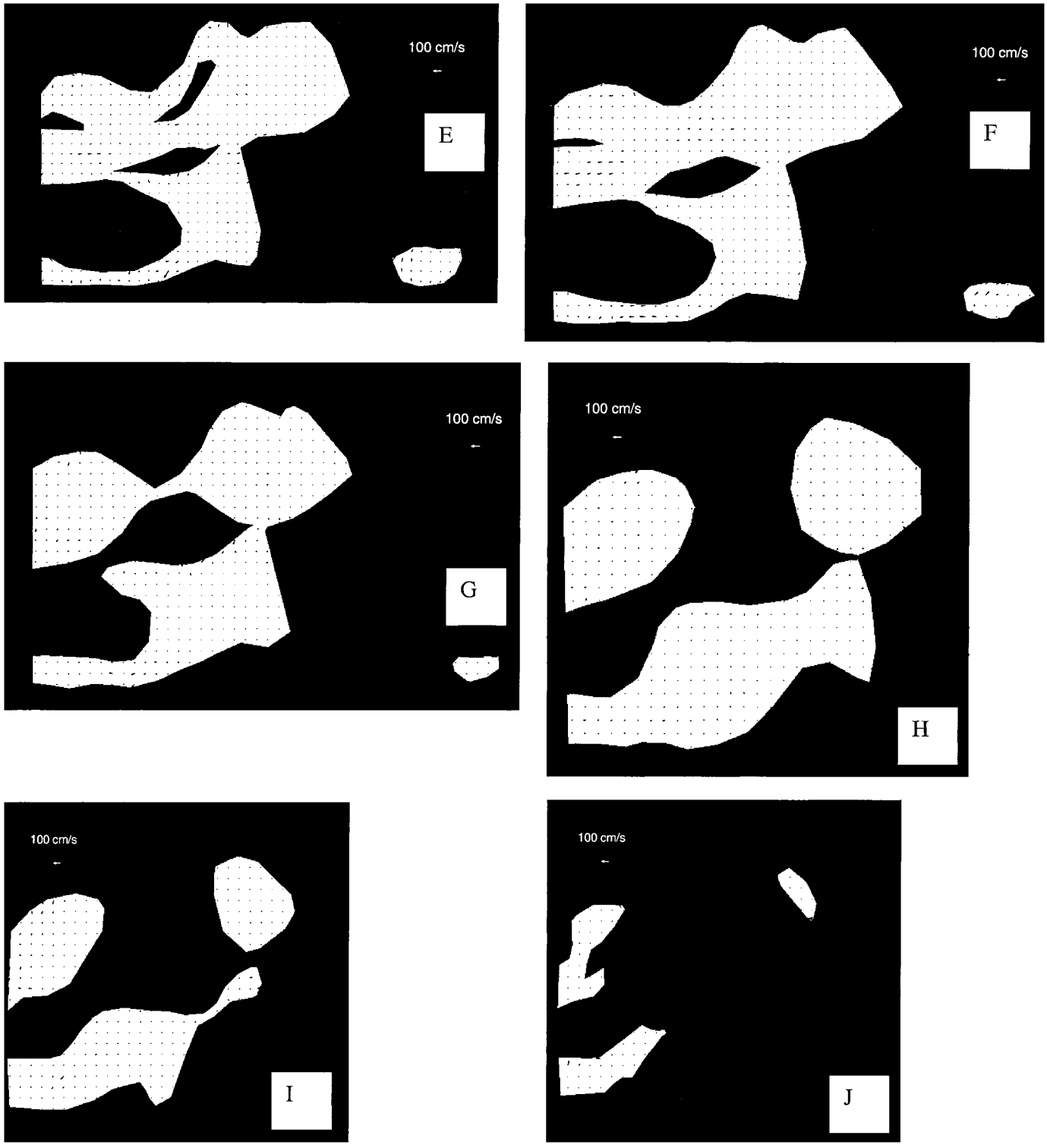

Fig. 11—*Continued.*

of the flow in this region than reported by Hahn et al. (5). It appears to be closer to the lower end of Stuiver's (20) observations, which is 5%. This discrepancy may be due to minor variations in dimension between the models studied. The vector plots presented by Park et al. (14) show a large fraction of the high-velocity flow to be in the olfactory slit. This may be due to the low resolution of anatomic data used for model creation, which seems to have resulted in a relatively large cross-sectional area in that region. The standing eddy in the olfactory area that was observed by Swift and Proctor (22) was not seen in this model. Differences in

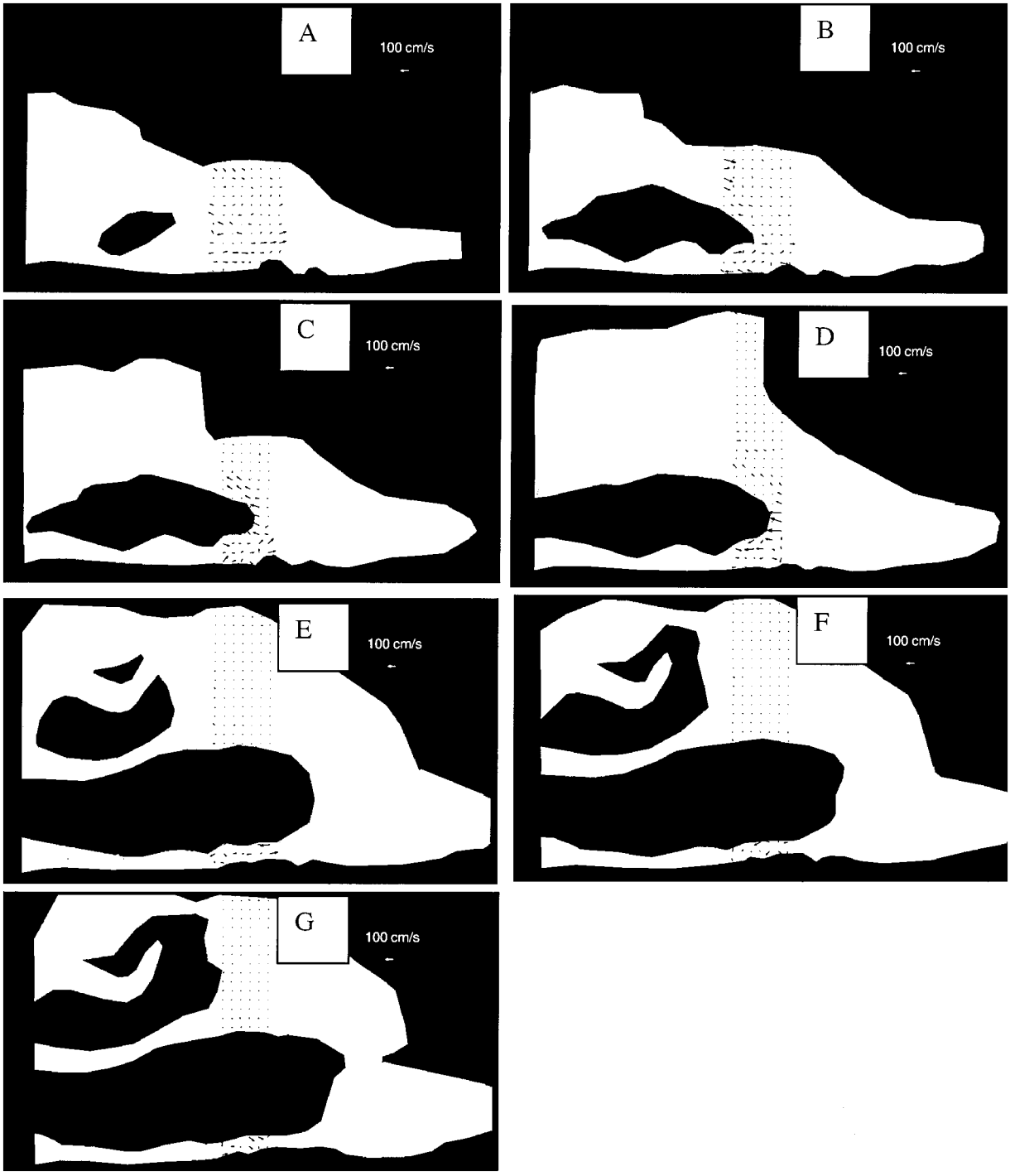

Fig. 12. Plots of vectors that represent the absolute difference of velocities between two coplanar vector plots in regions where they overlap, for a representative sample of data.

the model's anatomy, largely due to Swift and Proctor's use of a flat plate in place of the nasal septum, may be responsible for this flow variation.

Only a small fraction of the flow passed through the nasal meatuses. This phenomenon has been reported in previous studies. Proctor (16) determined that there was no significant change in airflow patterns in models when the meatuses were filled. Girardin et al. (4) reported that the majority of flow was close to the nasal septum. Schreck et al. (18) reported a low velocity in the meatuses. The velocity contour plots in Ref. 5 also depict relatively low flow in these airways.

Considering the low flow characteristic of the meatuses, the function of the turbinates does not appear to be one of particle filtration. The primary function of the turbinates is believed by many to be one of increasing the thermal and humidification capacity of the nasal cavity (8, 12, 13). The rich vascularity of the

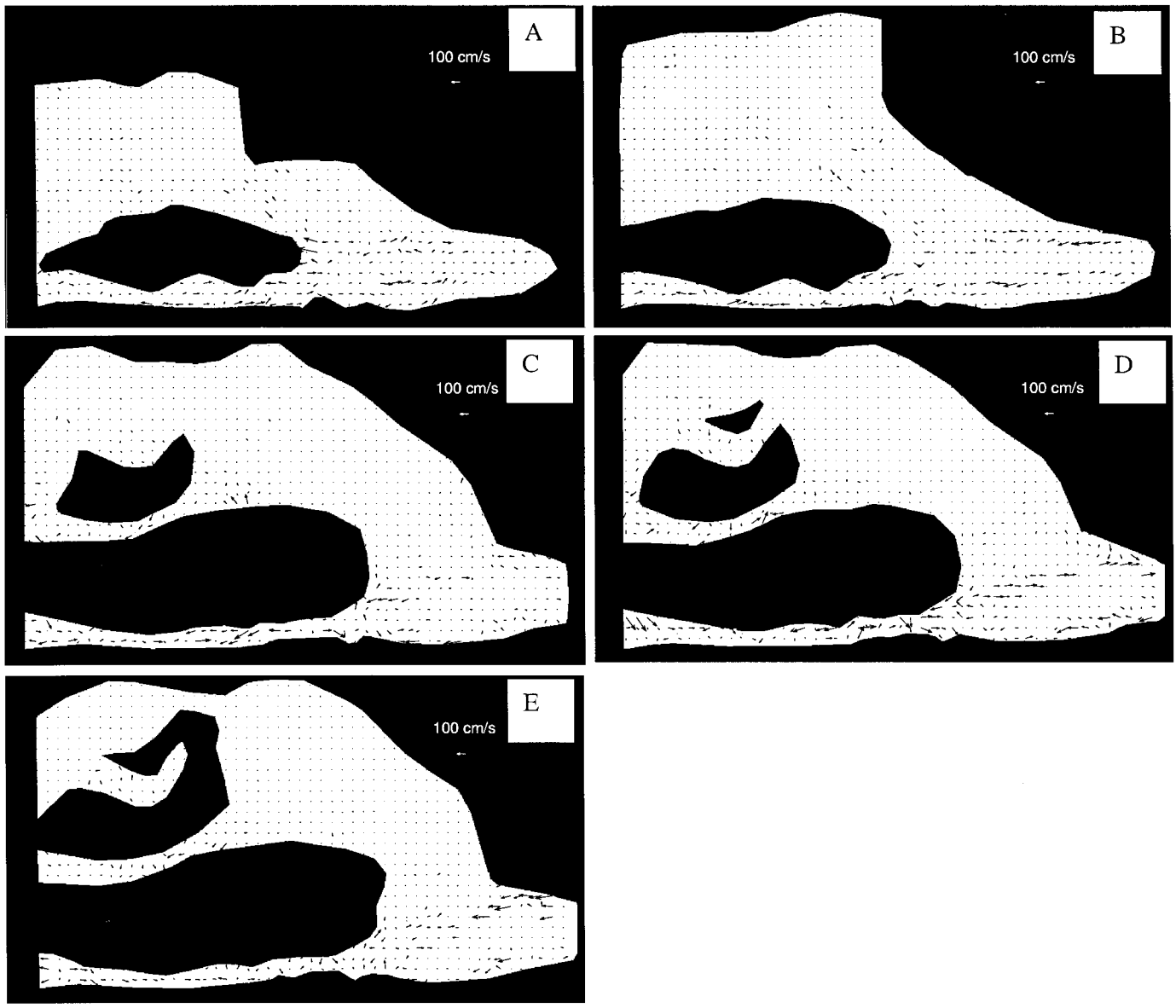

Fig. 13. Plots of vectors representing the absolute difference between velocity data acquired in the same plane at different times, for a representative sample of data.

turbinates (17) and the continual addition of airway secretions from the turbinate surfaces and sinuses to the surfaces in the main flow passage (16) are evidence that appear to support this belief. Also, a major concern in surgical removal of turbinate tissue is the possibility of subsequent nasal drying (8).

Scott (19), however, has suggested that the primary function of the turbinates may be one of thermoregulation of the body rather than air conditioning. He noted that many animals with complex turbinates live in temperate or tropical climates where simpler turbinates, such as those in humans, should sufficiently condition inspired air. He found that many of these animals are covered with dense hair and lack sweat glands, and he believed that their complex turbinates are necessary to regulate their body temperature. Cole (2) presented similar evidence that supports the view that the inferior turbinate in the human is a vestigial remnant of an organ concerned with heat and water economy, which is functionally significant in many other species.

The highest velocities were at the nasal valve and along the floor of the nasal cavity in the inferior airway. This finding was also reported in other studies and can be understood from geometric considerations. The nasal valve has the smallest cross-sectional area in the nasal cavity, and, as a consequence, there is high-velocity flow in that region. The flow leaving the nasal valve appears to experience the least resistance by flowing into the inferior airway, which explains the high-velocity flow there.

Keyhani et al. (9) and Subramaniam et al. (21) have performed computational fluid dynamics simulations of airflow in anatomically correct models of the nasal

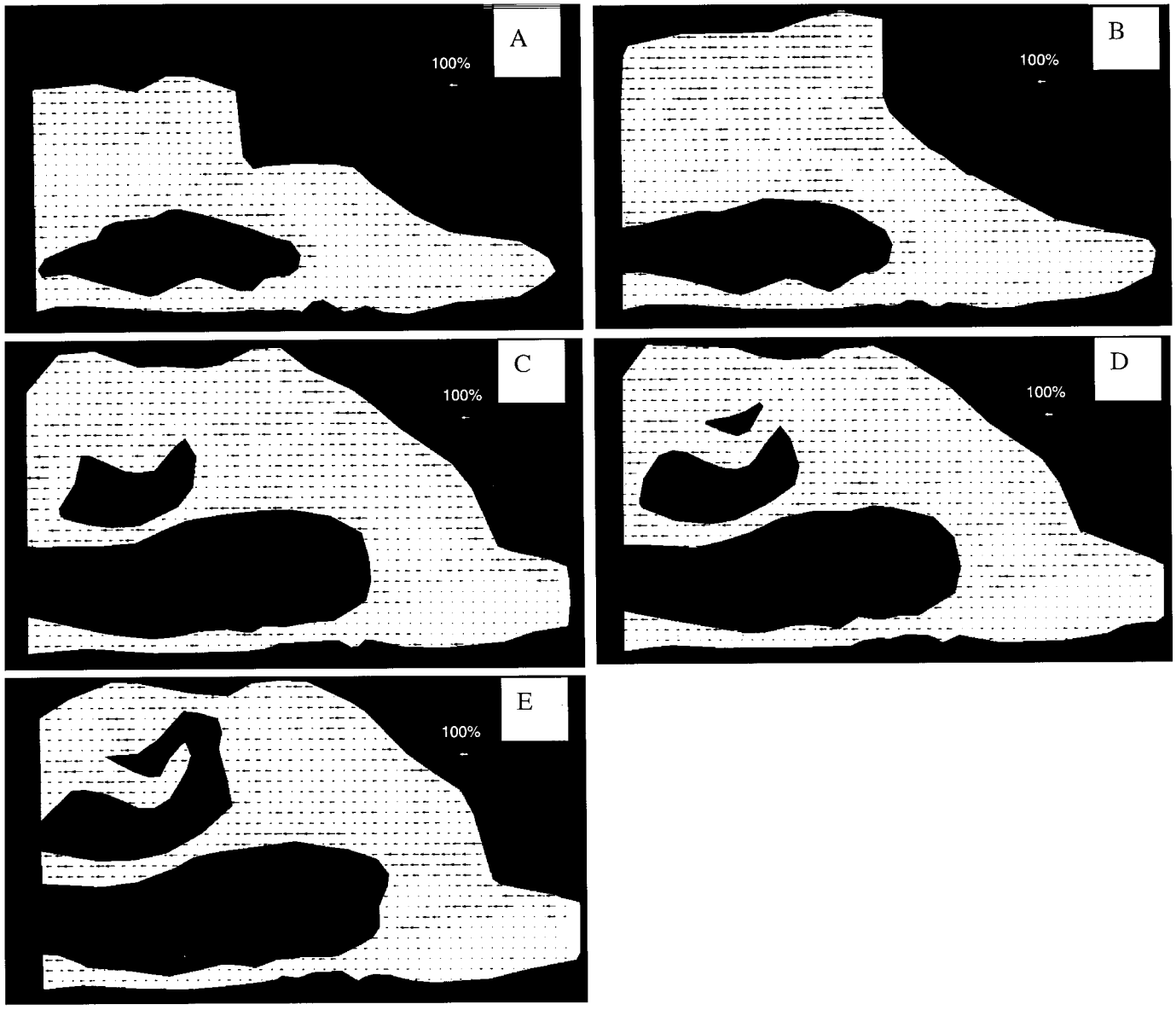

Fig. 14. Plots of vectors representing the difference between velocity data acquired in the same plane at different times, scaled according to associated velocity vector length, for a representative sample of data.

cavity. Keyhani et al. (9) reported that for a flow rate of 125 ml/s the highest airspeeds in the main nasal passages occurred along the nasal floor. The lowest airspeeds occurred in the superior regions of the nasal cavity and in the nasal meatuses. Subramaniam et al. (21) reported that, for a flow rate of 250 ml/s, the highest airspeeds in any coronal plane occurred in the lower or middle medial part of the cavity, with the highest airspeed being along the nasal floor. The fastest flow occurred in the posterior nasal valve region, and the olfactory region received only a small portion of the flow. It is not our intention to perform a rigorous comparison of our experiments with these simulations; however, gross flow distributions appear to be similar. Possible differences may include Keyhani et al. (9) observing a slightly larger portion of flow in the olfactory region than that observed here, which may be due to anatomic variations between models. Subramaniam et al. (21) reported a larger portion of flow in the middle meatus than was observed here. This disagreement may be associated with the differences in flow rates studied and anatomic variations between models.

Interindividual variations in nasal anatomy cause interindividual variations in nasal flow patterns, which are a concern when trying to use the results of a single cast or model. The general agreement of gross flow features in the variety of models studied suggests that some flow features are likely to remain unchanged for the population in general. These include high velocities along the nasal floor, in the nasal valve, and in the lower medial portion of the cavity, and low velocities in the olfactory slit and meatuses. However, the flow variations among different individuals have yet to be quantified.

The nasal cavity rapidly delivers oxygen to the lungs by limiting the majority of flow to a fraction of its passages. Finlike projections off these main flow passages, namely, the nasal meatuses and olfactory slit, seem to exist for thermal/humidification and olfaction purposes alone.

We thank Dr. K. R. Sreenivas for his contribution. We also thank the Electric Power Research Institute for sponsoring this work.

REFERENCES

1. **Adrian RJ.** Particle-imaging techniques for experimental fluid mechanics. *Ann Rev Fluid Mech* 23: 261–304, 1991.
2. **Cole P.** Nasal turbinate function. *Can J Otolaryngol* 2: 259–262, 1970.
3. **Eccles R.** Neurological and pharmacological considerations. In: *The Nose: Upper Airway Physiology and the Atmospheric Environment*, edited by Proctor DF and Anderson IB. New York: Elsevier, 1982, p. 191–214.
4. **Girardin M, Bilgen E, and Arbour P.** Experimental study of velocity fields in a human nasal fossa by laser anemometry. *Ann Otol Rhinol Laryngol* 92: 231–236, 1983.
5. **Hahn I, Scherer PW, and Mozell MM.** Velocity profiles measured for airflow through a large-scale model of the human nasal cavity. *J Appl Physiol* 75: 2273–2287, 1993.
6. **Hopkins LM, Kelly JT, Prasad AK, and Wexler AS.** Particle image velocimetry measurements in complex geometries. *Exp Fluids* 29: 91–95, 2000.
7. **Hornung DE, Leopold DA, Youngentob SL, Sheehe PR, Gagne GM, Thomas FD, and Mozell MM.** Airflow patterns in a human nasal model. *Arch Otolaryngol Head Neck Surg* 113: 169–172, 1987.
8. **Jackson LE and Koch RJ.** Controversies in the management of inferior turbinate hypertrophy: a comprehensive review. *Plast Reconstr Surg* 103: 300–312, 1999.
9. **Keyhani K, Scherer PW, and Mozell MM.** Numerical simulation of airflow in the human nasal cavity. *J Biomech Eng* 117: 429–441, 1995.
10. **Masing H.** Investigations about the course of flow in the nose model. *Arch Klin Exp Ohren Nasen Kehlkopfheilkd* 189: 371–381, 1967.
11. **Miner CS and Dalton NN.** *Glycerol*. New York: Reinhold, 1953, p. 280.
12. **Naftali S, Schroter RC, Shiner RJ, and Elad D.** Transport phenomena in the human nasal cavity: a computational model. *Ann Biomed Eng* 26: 831–839, 1998.
13. **Nunn JF.** *Nunn's Applied Respiratory Physiology* (4th ed.). Oxford, UK: Butterworth-Heinemann, 1993, p. 13.
14. **Park KI, Brucker C, and Limberg W.** Experimental study of velocity fields in a model of human nasal cavity by DPIV. In: *Laser Anemometry Advances and Applications: Proceedings of the 7th International Conference,* edited by Ruck B, Leder A, and Dopheide D. Karlsruhe, Germany: University of Karlsruhe, 1997.
15. **Prasad AK and Adrian RJ.** Stereoscopic particle image velocimetry applied to liquid flows. *Exp Fluids* 15: 49–60, 1993.
16. **Proctor DF.** The upper airway. In: *The Nose: Upper Airway Physiology and the Atmospheric Environment*, edited by Proctor DF and Anderson IB. New York: Elsevier, 1982, p. 23–43.
17. **Ritter FN.** Vasculature of the nose. *Ann Otol Rhinol Laryngol* 79: 468–474, 1970.
18. **Schreck S, Sullivan KJ, Ho CM, and Chang HK.** Correlations between flow resistance and geometry in a model of the human nose. *J Appl Physiol* 75: 1767–1775, 1993.
19. **Scott JH.** The comparative anatomy and function of the maxillary turbinate. *J Anat* 87: 461–462, 1953.
20. **Stuiver M.** *Biophysics of the Sense of Smell* (PhD thesis). Groningen, The Netherlands: Rijks University, 1958.
21. **Subramaniam RP, Richardson RB, Morgan KT, Kimbell JS, and Guilmette RA.** Computational fluid dynamics simulations of inspiratory airflow in the human nose and nasopharynx. *Inhal Toxicol* 10: 473–502, 1998.
22. **Swift DL and Proctor DF.** Access of air to the respiratory tract. In: *Respiratory Defense Mechanisms: Part I*, edited by Brain JD, Proctor DF, and Reid LM. New York: Dekker, 1977, p. 63–93.